

A Classical Analysis of Capacitively Coupled Superconducting Qubits

James A. Blackburn¹, Jeffrey E. Marchese², Matteo Cirillo³, and Niels Grønbech-Jensen²

¹*Department of Physics & Computer Science, Wilfrid Laurier University, Waterloo, Ontario N2L 3C5, Canada*

²*Department of Applied Science, University of California, Davis, California 95616 and*

³*Dipartimento di Fisica and MINAS-Lab, Università di Roma "Tor Vergata", I-00173 Roma, Italy*

An electrical circuit consisting of two capacitively coupled inductive loops, each interrupted by a Josephson junction, is analyzed through the classical RCSJ model. The same circuit has recently been studied experimentally and the results were used to demonstrate quantum mechanical entanglement in the system by observing the correlated states of the two inductive loops after initial microwave perturbations. Our classical analysis shows that the observed phenomenon exists entirely within the classical RCSJ model, and we provide a detailed intuitive description of the transient dynamics responsible for the observations.

I. INTRODUCTION

In 2005, McDermott et al. [1] reported the experimental observation of quantum mechanical entanglement in a system of two qubits, each comprised of a superconducting loop interrupted by a single underdamped Josephson junction, and weakly coupled via a capacitor. A second report with some additional detail soon followed [2], and a review by Siddiqi and Clarke [3] of the key ideas appeared in that same issue of Science.

Briefly, the model put forward to explain the experimental observations was as follows. The potential energy of a superconducting ring interrupted by a Josephson junction, plotted as a function of the junction phase variable, can possess a shallow well if biased with an appropriate magnetic field. Quantum mechanics dictates discrete energy levels within a finite well, and a sufficiently shallow well would have just a few permitted bound states, of which the two lowest are denoted $|0\rangle$, $|1\rangle$. The argument has been advanced that such a system can be viewed as a fictitious particle being limited to these quantum states [4], rather than, as in a “classical” picture, freely exploring the potential surface. This distinction is crucial to what follows.

In the experiments, two loops were subjected to a steady flux bias that made the occupied wells shallow. One of the loops was given additional time-dependent flux biasing in the form of a 10 ns microwave burst. The microwave frequency was set to match the separation of the two levels within the driven well, so it was imagined that the pulse would selectively populate the first excited state of the driven loop, initially putting the coupled system in the $|01\rangle$ state. Then, after a “free evolution time” during which the qubits interact, the states of both loops were probed using identical measurement pulses of exactly the correct amplitude to reduce the barrier and facilitate selective tunneling (or, more precisely, Macroscopic Quantum Tunneling (MQT)) out of the upper state $|1\rangle$, but not out of the lower state $|0\rangle$. Hence, if either well were in an excited state, then escape via tunneling would lead to time dependent phase dynamics and a resulting observed signal; if it were in the lower state, no signal would be seen. This probing was repeated many

times for each selected t_{free} and the accumulated data were argued to reveal the probabilities for $|00\rangle$, $|01\rangle$, $|10\rangle$, and $|11\rangle$, and to confirm that entanglement had been observed.

We here provide a classical Resistively and Capacitively Shunted Junction (RCSJ) analysis of the capacitively coupled qubit system. This builds upon our previous work which has reproduced several experimental observations, such as those seen in [5], including: multi-peaked distributions [6], Rabi-oscillations [7], Ramsey fringes [8], and spin-echo [9]. In this model the microwave pulse stimulates small phase oscillations in the driven loop and, because of the coupling, the passive loop soon develops its own phase oscillations. Thus we study a straightforward picture – that of a pair of weakly coupled oscillators. Our analysis shows that these coupled phase oscillations can yield very good quantitative agreement with the core of experimental observations. It also points to the crucial role of thermal noise in this system.

II. THE MODEL

We begin with the circuit shown in Fig. 1. Each junction is characterized by a critical current I_c , resistance R , and capacitance C ; each loop has an inductance L . The two loops are coupled through a capacitance C_X . Let Φ_{1x} be the externally applied flux on Loop #1 and Φ_{2x} be the externally applied flux on Loop #2. With overdots denoting derivatives in dimensionless time $\tau = \omega_J t$, and with the junction plasma frequency $\omega_J = \sqrt{2eI_c/\hbar C}$, the resulting equations of motion for the two junction phases can be shown to be

$$\ddot{\varphi}_1 + \alpha\dot{\varphi}_1 + \sin\varphi_1 = \gamma_x(\ddot{\varphi}_2 - \ddot{\varphi}_1) - \beta_L^{-1}(\varphi_1 + 2\pi M_{1x}) \quad (1)$$

$$\ddot{\varphi}_2 + \alpha\dot{\varphi}_2 + \sin\varphi_2 = \gamma_x(\ddot{\varphi}_1 - \ddot{\varphi}_2) - \beta_L^{-1}(\varphi_2 + 2\pi M_{2x}) \quad (2)$$

where $\alpha = 1/\omega_J CR$, and $\beta_L = 2\pi LI_c/\Phi_0$; Φ_0 being the flux quantum. $M_{ix} = \Phi_{ix}/\Phi_0$ is the normalized applied flux through loop i and the mutual coupling coefficient is $\gamma_x = C_x/C$. The characteristic energy of this system

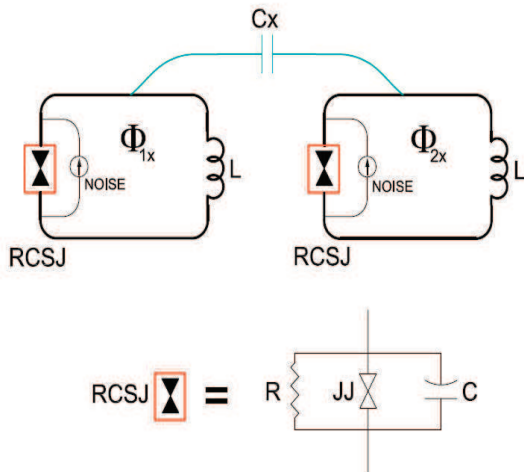


FIG. 1: Configuration of two capacitively coupled superconducting loops, each containing a Josephson junction represented by the RCSJ equivalent circuit and an associated noise source.

is $E_J = I_c \Phi_0 / 2\pi$. The equations of motion can also be put in the convenient form,

$$\ddot{\varphi}_a + \alpha \dot{\varphi}_a + \sin \varphi_a \cos \varphi_b = -\beta_L^{-1} [\varphi_a + 2\pi M_a] \quad (3)$$

$$g^{-1} \ddot{\varphi}_b + \alpha \dot{\varphi}_b + \sin \varphi_b \cos \varphi_a = -\beta_L^{-1} [\varphi_b + 2\pi M_b], \quad (4)$$

where $\varphi_a = (\varphi_1 + \varphi_2)/2$ and $\varphi_b = (\varphi_1 - \varphi_2)/2$ are transformed variables, and $M_a = (M_{1x} + M_{2x})/2$, $M_b = (M_{1x} - M_{2x})/2$, and $g^{-1} = 1 + 2\gamma_x$ are the corresponding magnetic fields and coupling, respectively. Based on published data, we set the parameters at $\alpha = 5 \times 10^{-5}$ (very light damping), $\beta_L = 2.841$, and $g = 0.9954$, $I_c = 1.1 \mu\text{A}$, $C = 1.3 \text{ pF}$, $\omega_J^{-1} = 0.02 \text{ ns}$. Both loops are biased with a dc flux 0.6941 (resonance $\approx 5.1 \text{ GHz}$) and with superimposed pulses as shown in the upper panel of Fig.2.

III. SIMULATION RESULTS

We have numerically solved the coupled equations (3) and (4) using both fourth order Runge-Kutta and Verlet algorithms. Simulations at zero temperature were conducted as follows.

The duration of the microwave burst was set at 100 plasma periods; the amplitude and normalized frequency were 0.000580 and 0.989, respectively. Our results are shown in the three lower panels of Fig.2. In each plot, the darker trace is the phase in Loop #2. The effect of the microwave burst is easily seen – the phase φ_2 is kicked into rapid oscillations around its initial rest value of -1.52 rad . These oscillations continue after the microwave burst has ended. Because of the coupling, the phase in Loop #1 also oscillates. Furthermore, in a manner characteristic of weakly coupled oscillators [10], each waveform has the appearance of an amplitude modulated carrier, and the envelope of one is exactly out of

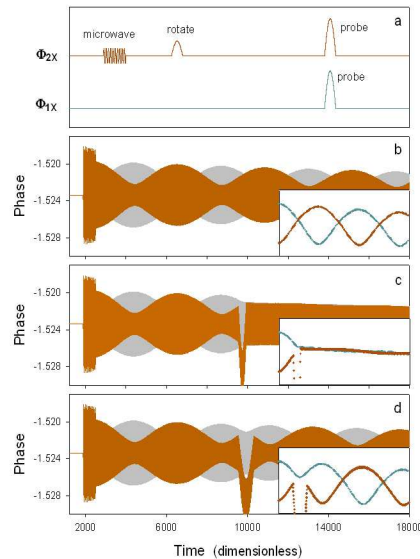


FIG. 2: (a) Bias sequence for the two loops (not to scale). (b)-(d) Numerical solutions of the coupled loop equations. In each plot, the darker wave form is for Loop #2, the lighter for Loop #1. In (c) and (d), a rotation pulse is applied at time 9550. The insets show portions of the upper envelopes of the modulated phase oscillations.

phase with the other. Note that the amplitude of these modulations is very small compared to the dc level. The junction phase oscillations are so rapid (the frequency ratio of carrier to modulation is about 400:1) that on the scale of this figure they become compressed into solid shading.

A rotation pulse of amplitude 0.000915 was applied at time 9550. For these simulations, we chose widths of 0, 60, and 120 plasma periods, equivalent to 0 ns, 7.5 ns, and 15 ns. The insets in each of the three panels show the upper modulation envelopes as functions of time and their responses to the different rotation pulse widths. The significance of these plots is their exact matching to the time dependence of the experimental probabilities P_{01} and P_{10} given in Fig. 2B,C,D of [2]. Steffen et al. say: “The occupation probabilities P_{01} and P_{10} oscillate out of phase with a period of 100 ns, consistent with the spectroscopic measurements.” Our numerical results exhibit the same shapes and phase relationships for the envelopes. As well, our simulation data show the period of the envelopes to be 87 ns. In other words, the modulation envelopes that are a natural outcome of the classical physics of weakly coupled oscillators are a match to the experimental data, and the underlying dynamical phenomena of both the modulation and the results of manipulation observed in Ref. [2] are well represented in the RCSJ model.

The experiments reported in [2] were conducted at 25 mK. Following their experimental protocols, we added

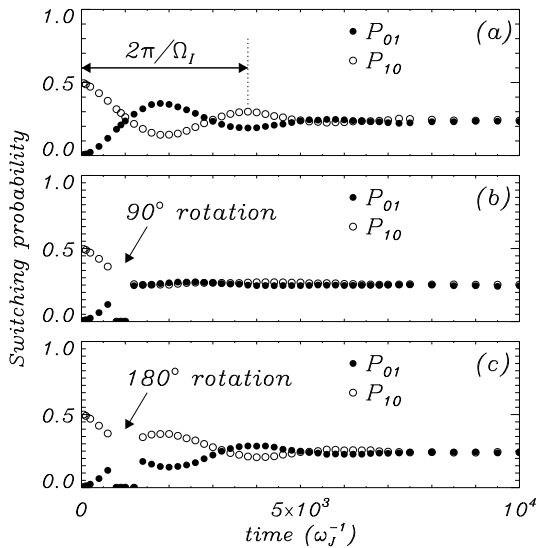


FIG. 3: Numerical simulations for $T = 25 \text{ mK}$ with thermalization time of 10^3 time units, and $\alpha = 5 \times 10^{-5}$. Pulsed microwave frequency is 0.625, and pulse duration and amplitude are 507 and 0.00058, respectively. Each marker represents an average of 1,000 measurements conducted with a triangular probe pulse of amplitude 0.0538 and width 500. (b) and (c) rotation pulse application time is 818.75 after termination of the microwave, and rotation amplitude is 0.000915. (b) 90° rotation pulse duration is 253.5. (c) 180° rotation pulse duration is 507.

appropriate noise to the system equations (3) and (4), simulating 25 mK thermal noise with a short transient time of 1,000 time units. For any chosen moment following the microwave burst (t_{free}), repeated simulation runs were carried out and data were gathered on how often the individual loops experienced an escape following the application of the probe pulse (amplitude 0.0358). The results are shown in Fig.3. The close correspondence with the reported experimental results in [2] is obvious.

Comparing Fig.2 and Fig.3, it is apparent that in combination with noise, the probe pulse effectively ‘teases out’ the modulation profiles of the junction phase oscillations. Equivalently, the likelihood that the ‘particle’ will escape from its well will be higher at moments when the noise-free oscillation amplitude (energy) is relatively large, and conversely, when the oscillation amplitude is small, the chance of escape is less. Hence the classical description of the system, embodied in Eqs.(3,4) captures all the significant features observed in the experiments. However, there is a wrinkle in the above picture that we

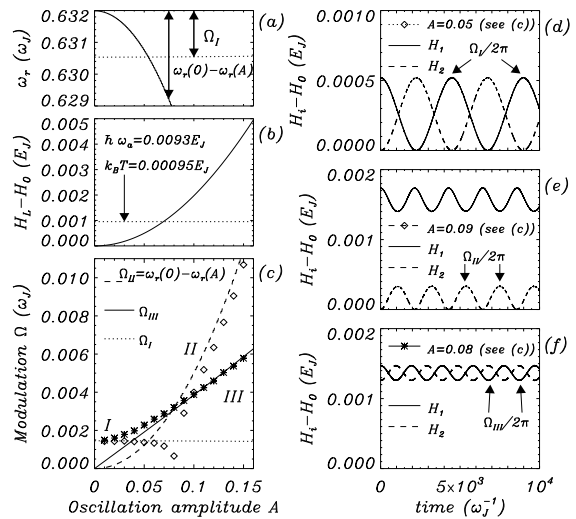


FIG. 4: Analyses of system modes with parameters given in the text. Single loop resonance (a) and energy (b) as a function of oscillation amplitude A . (c) Modulation frequencies; simulated (markers) and perturbation analysis (lines). Different modes are engineered through the initial conditions $\varphi_i(0) = \varphi_0 + A_i$ such that mode-I is obtained by $A_1 = A$ (small) and $A_2 = 0$, mode-II by $A_1 = A$ (large) and $A_2 = 0$, and mode-III by $A_1 \approx A_2$ (large). Examples of the three characteristic modes observed in (c): mode-I (d), mode-II (e), and mode-III (f).

will discuss after having identified the dynamical modes in the system.

IV. PERTURBATION ANALYSIS

Let us first provide a simple analysis for the *single* qubit. Inserting the ansatz $\varphi = \varphi_0 + A \sin \omega t$ into Eq. (1) for $\gamma_x = 0$ we get the following relationships between the fixed phase φ_0 and the resonance frequency ω_r to the magnetic field M_x and amplitude A of oscillation:

$$\omega_r^2 = \beta_L^{-1} + (J_0(A) + J_2(A)) \cos \varphi_0 \quad (5)$$

where

$$J_0(A)\beta_L \sin \varphi_0 = -\varphi_0 - 2\pi M_x.$$

The latter expression provides the mean phase φ_0 , while the former Eq.(5) is the anharmonic resonance shown in Fig.4a for small to moderate oscillation amplitudes.

With this parameterized ansatz, we can provide the energy H_L of a single qubit as the averaged sum of kinetic energy and potential energy $U(\varphi) = 1 - \cos \varphi + [\varphi +$

$$2\pi M_x]^2/2\beta_L$$

$$H_L = \langle \frac{1}{2}\dot{\varphi}^2 + U(\varphi) \rangle = \frac{1}{4}A^2\omega^2 + \frac{1}{4\beta_L}A^2 + 1 - J_0(A) \cos \varphi_0 + \frac{1}{2\beta_L}[\varphi_0 + 2\pi M_x]^2 \quad (6)$$

This energy is shown in Fig.4b for the upper of the two potential wells of the qubit potential. Notice that the energy of the fixed-point is $H_0 = U(\varphi_0)$. With these basic anharmonic relationships we can now proceed to analyzing the inherent *system* resonances.

Mode-I: beat frequency mode. In Eqs. (3) and (4), with $M_b = 0$, $\alpha \approx 0$, and small amplitude oscillations of φ_1 and φ_2 , we write $\varphi_a = \varphi_0 + \psi_a$, where φ_0 is a constant and $|\psi_a| \ll 1$, and we will similarly assume $|\varphi_b| \ll 1$. Inserting this ansatz with $\alpha = 0$ (for simplicity) gives the linear equations

$$\ddot{\psi}_a + \sin \varphi_0 + (\cos \varphi_0 + \beta_L^{-1})\psi_a + \beta_L^{-1}(\varphi_0 + 2\pi M_x) = 0 \quad (7)$$

$$g^{-1}\ddot{\varphi}_b + (\cos \varphi_0 + \beta_L^{-1})\varphi_b = 0. \quad (8)$$

From this we directly obtain $\beta_L \sin \varphi_0 + \varphi_0 + 2\pi M_x = 0$, and we get the linear resonance frequencies ω_a and ω_b of ψ_a and φ_b , respectively, as $\omega_a^2 = \cos \varphi_0 + \beta_L^{-1}$ and $\omega_b^2 = g\omega_a^2$. Thus, in addition to the microwave carrier frequency $\approx \omega_a$, we see a modulation frequency at

$$\Omega_I = \omega_a - \omega_b = (1 - \sqrt{g})\omega_a, \quad (9)$$

which, with the reported experimental parameters, is given by $\omega_a \approx 0.63199$ and $\Omega_I \approx 0.001455$. Notice that $2\pi/\Omega_I$ is the exact modulation period (86.4ns) observed in both experiments and simulations. The energy modulation of this mode is exemplified in Fig.4d.

Mode-II: phase-slip mode. A direct consequence of the anharmonicity of the system is that mode-I can only exist for low system energy. The reason is that the two different oscillation amplitudes (A_1, A_2) observed in Fig.4d give rise to two different resonance frequencies seen in Eq. (5) and Fig.4a. Thus, the linear mode-I cannot exist if the disparity between the resonance frequencies overwhelms the linear modulation frequency Ω_I . If that happens, then the two oscillators will shift to a mode-II, where the two loops will advance in two different energy and frequency states, as illustrated in Fig.4e. The observed energy modulation is a result of the mutual phase-slip between the oscillators, which for systems of different oscillation amplitudes $A_1 > A_2$ can be approximated by

$$\Omega_{II} \approx \omega_r(A_2) - \omega_r(A_1). \quad (10)$$

Mode-III: phase locked mode. This is a mode, illustrated in Fig.4f, which can be analyzed similarly to the classical Rabi-type oscillation outlined in Ref. [7]. We define the ansatz $\varphi_i = \varphi_0(A_i) + A_i \sin(\omega_r(A_i)t + \theta_i)$ ($i = 1, 2$), $A_1 \approx A_2 \approx A$, and $\theta_1 = -\theta_2$. Considering the energy flow into qubit #1 from the coupling,

$$\dot{H}_1 = \gamma_x \dot{\varphi}_1 (\ddot{\varphi}_2 - \ddot{\varphi}_1) \quad (11)$$

$$\approx A\omega_r \cos(\omega_r t + \theta_1) \times [A\omega_r^2 \sin(\omega_r t + \theta_1) - A\omega_r^2 \sin(\omega_r t - \theta_1)], \quad (12)$$

we write the energy H_1 of qubit #1 using Eq. (6). The energy change ΔH_1 of qubit #1 over one time unit can therefore be expressed

$$\Delta H_1 = \frac{\partial H_1}{\partial t} = \frac{\partial H_1}{\partial A_1} \frac{\partial A}{\partial \omega_r} \ddot{\theta}_1 = \langle \dot{H}_1 \rangle = \frac{1}{2} \gamma_x A_1^2 \omega_r^3 \sin(2\theta_1) \quad (13)$$

$$\Rightarrow \frac{\partial H_1}{\partial A_1} \frac{\partial A}{\partial \omega_r} \ddot{\theta}_1 \approx \gamma_x A_1^2 \omega_r^3 \theta_1 \quad (14)$$

for $|\theta_1| \ll 1$. This provides a slow modulation frequency

$$\Omega_{III} = \sqrt{-\gamma_x A^2 \omega^3 \frac{\partial \omega}{\partial A} / \frac{\partial H_1}{\partial A}}, \quad (15)$$

where we note that $\partial \omega / \partial A < 0$.

The above perturbation analysis provides definite expectations for the type of excitations one can expect and how they relate to the experimental observations. Judging from Figs.4d-f, we infer that only mode-I can be the experimentally observed, due to the statements in Ref. [2] about using identical probe pulses to get the presented high resolution and fidelity. The complexity of the modulation resonances are shown in Fig.4c with comparisons between evaluated modulation frequencies and direct numerical simulations for $\alpha = 0$ as a function of oscillation amplitudes. We see that mode-I is always present for small A , and that it is never present for large A due to the anharmonic modes II and III. The transition to the anharmonic modes appears at a system energy given by the the magnitude of A – see Figs.4c and 4b, where we have also indicated the energy level of 25mK. It is here apparent that mode-I does not exist with energy content much larger than the thermal energy for the given system parameters. We have numerically verified this for a fully thermalized system at 25mK. Only if not fully thermalized (as is the case for Fig.3 above) or at thermodynamic temperatures below 3mK do we observe mode-I.

V. DISCUSSION

We note that results of the classical model depend on the choice of the phenomenological damping parameter α , which is not directly given by the experimental data

in [2]. The inverse of this parameter relates to both the decay time for coherent signals in the system and the characteristic time of thermalization; the value of this parameter is therefore a significant component to understanding the system behavior. For this presentation we have chosen a very small value of damping in line with the observed decay times of the modulations as well as with the assumed large sub-gap resistance associated with high quality aluminum junctions at the very low temperature used for the experiments.

With the long history of the RCSJ model explaining experimental observations, as outlined in the introduction, it is natural to approach any new configuration from the same starting point. For the present system, such direct classical analysis provides excellent agreement with

what is actually seen in the experiments, as illustrated in Figs.2 and 3. However, our analysis also points to a still unresolved question of thermal effects and the stability of the relevant modes in the balance between temperature and anharmonicity.

Acknowledgments

We are grateful for useful discussions with M. R. Samuelsen. This work was supported in part (JAB) by a grant from the Natural Sciences and Engineering Research Council of Canada.

-
- [1] R. McDermott, R.W. Simmonds, M. Steffen, K.B. Cooper, K. Cicak, K.D. Osborn, S. Oh, D.P. Pappas, J.M. Martinis, *Science* **307**, 1299 (2005).
 - [2] M. Steffen, M. Ansmann, R. C. Bialczak, N. Katz, E. Lucero, R. McDermott, M. Neeley, E.M. Weig, A.N. Cleland, J.M. Martinis, *Science* **313**, 1423 (2006)
 - [3] I. Siddiqi and J. Clarke, *Science* **313**, 1400 (2006)
 - [4] J. Clarke, A.N. Cleland, M.H. Devoret, D. Esteve, J.M. Martinis, *Science* **239**, 992 (1988)
 - [5] see, e.g., D. Vion, A. Aassime, A. Cottet, P. Joyez, H. Pothier, C. Urbina, D. Esteve, and M.H. Devoret, *Forsch. Phys.* **51**, 462 (2003).
 - [6] N. Grønbech-Jensen, M. G. Castellano, F. Chiarello, M. Cirillo, C. Cosmelli, L. Fillipenko, R. Russo, and G. Torrioli, *Phys. Rev. Lett.* **93**, 107002 (2004); N. Grønbech-Jensen, M. G. Castellano, F. Chiarello, M. Cirillo, C. Cosmelli, V. Merlo, R. Russo, and G. Torrioli, in *Quantum Computing: Solid State Systems*, Eds. B. Ruggiero, P. Delsing, C. Granata, Y. Paskin, and P. Silvestrini (Kluwer Academic/Springer, New York, 2006), pp. 111-119; N. Grønbech-Jensen and M. Cirillo, *Phys. Rev. B* **70**, 214507 (2004).
 - [7] N. Grønbech-Jensen and M. Cirillo, *Phys. Rev. Lett.* **95**, 067001 (2005); J. E. Marchese, M. Cirillo, and N. Grønbech-Jensen, *Phys. Rev. B* **73**, 174507 (2006); J.M. Marchese, Ph.D. Thesis, The University of California, Davis (2007).
 - [8] J. E. Marchese, M. Cirillo, and N. Grønbech-Jensen, *Open Sys.& Inf. Dyn.* **14**, 189 (2007); see also Ref. [9].
 - [9] J. E. Marchese, M. Cirillo, and N. Grønbech-Jensen, *Eur. Phys. J.* **147**, 333 (2007).
 - [10] T.L. Chow, *Classical Mechanics* (Wiley 1995), see pp.394,395